Polyoxometalate-Based Layered Structures for Charge Transport Control in Molecular Devices

Antonios M. Douvas,[†,*] Eleni Makarona,[†] Nikos Glezos,[†] Panagiotis Argitis,[†] Jerzy A. Mielczarski,[‡] and Ela Mielczarski[‡]

[†]Institute of Microelectronics, National Center of Scientific Research "Demokritos", 15310 Aghia Paraskevi, Athens, Greece, and [‡]LEM, INPL/CNRS, UMR 7569, B.P. 40, 54501 Vandoeuvre-lès-Nancy, France

ABSTRACT Hybrid organic–inorganic films consisted of molecular layers of a Keggin-structure polyoxometalate (POM: 12-tungstophosphoric acid, $H_3PW_{12}O_{40}$) and 1,12-diaminododecane (DD) on 3-aminopropyl triethoxysilane (APTES)-modified silicon surface, fabricated *via* the layer-by-layer (LBL) self-assembly method are evaluated as molecular materials for electronic devices. The effect of the fabrication process parameters, including primarily compositions of deposition solutions, on the structural characteristics of the POM-based multilayers was studied extensively with a combination of spectroscopic methods (UV, FTIR, and XPS). Well-characterized POM-based films (both single-layers and multilayers) in a controlled and reproducible way were obtained. The conduction mechanisms in single-layered and multilayered structures were elucidated by the electrical characterization of the produced films supported by the appropriate theoretical analysis. Fowler—Nordheim (FN) tunneling and percolation mechanisms were encountered in good correlation with the structural characteristics of the films encouraging further investigation on the use of these materials in electronic and, in particular, in memory devices.

KEYWORDS: molecular electronics · monolayers · polyoxometalates · layer-by-layer self-assembly method · hybrid molecular materials.

Using individual molecules as the smallest possible electrical elements in devices has undoubtedly the potential to revolutionize modern technologies. An intense research activity has therefore been concentrated on developing new molecular-based materials with electron-transport and/or electron-storage properties necessary for decreasing the size of the components of future electronic devices down to nano- and subnanometer dimensions or for novel applications. The successful implementation of molecules in electronic devices depends to a great extent on our controlling of the material's structural parameters and on our understanding of the intricate electron-transport phenomena accompanying molecular conductance.[1–3]

A wide variety of molecular materials with different chemical and structural characteristics have been proposed for potential use in electronics applications.[4,5] In this context, the study of hybrid organic–inorganic ultrathin films based on polyoxometalates (POMs), that is, compounds that can be envisioned as molecular metal–oxygen anionic clusters,[6–11] has drawn considerable and increasing attention. Particularly, POMs with Keggin structure[10–15] have been mostly selected, because of their important—for electronic and related applications—characteristic to accept one or more electrons without significant structural changes and to delocalize these electrons over several metal centers of their framework.[7,8,10,11,16–19] In addition, these POMs exhibit good solubility in a wide variety of solvents and stability toward oxidation both in solution and in solid state,[10,11] whereas they are easily synthesized, and some are commercially available. Thus, POM-based materials (especially their optical,[20,21] electrochemical,[22] photochromic,[23,24] electrochromic,[25] and magnetic properties[26]) have been studied extensively and they have been suggested as promising components of devices since 1998.[27,28] Organized POM-based hybrid materials have been formed as alternate monolayers of anionic POMs and cationic organic molecules such as polyelectrolytes,[29] porphyrins,[30] dyes,[31] or long alkyl chain amines,[32,33] using the layer-by-layer (LBL) self-assembly method.[34] On the other hand, the fabrication of similar materials with the use of amphiphilic organic molecules *via* the Langmuir–Blodgett method[35] has also been reported.[36]

The electron transport properties of POM-based films and their potential use in memory or other type of electronic devices have been studied during the past few years by our group and recently other groups.[37] The previous work of our group

*Address correspondence to adouvas@imel.demokritos.gr.

Received for review October 29, 2007 and accepted February 22, 2008.

Published online March 18, 2008.
10.1021/nn700333j CCC: $40.75

was mainly concentrated on POMs (especially tungstates) embedded into polymeric (*e.g.*, poly(methyl methacrylate), PMMA) films.[38,39] Using planar nanoelectrodes voltage plateaus and charge hysterisis effects were observed and attributed to electron trapping by POMs and to tunneling mechanisms. Quantum tunneling effects were evident in the case of small electrode distance and high molecular concentration, as resulted from the tunneling analysis performed. This study concluded that the selective charging of tungstates can be exploited in future memory devices. At this point it should be further emphasized that POMs with Keggin structure have also some significant—mainly for electronic applications—characteristics: (i) well-defined molecular structure with a size of ~1 nm, and consequent classification as zero-dimensional semiconductors;[14,40] (ii) low charging energies (from the Fermi level of Al or Au electrode to their lowest unoccupied molecular orbital, LUMO, level) in the range of 0.1−0.4 eV, and therefore resolution of discrete electronic levels at room temperature; and (iii) n-type conductivity and its resemblance with the conductivity of large organic molecules (such as fullerenes)[41] and metal nanoclusters,[40,42] which are closer to materials that have been used so far in electronics applications.

To further exploit the potential of these molecular materials as components of electronic devices we proceeded with the study of hybrid POM-based multilayers. In a first paper, we reported hybrid films prepared and examined as dielectric components in silicon-based capacitance structures.[43] The dependence of charging upon the structure of the layer was demonstrated, and the distance between the active molecules was estimated.

In the present work, a systematic study of the charge transport mechanisms involved in hybrid POM-based multilayers in relation with the film structural characteristics is performed. The multilayer films consist of a Keggin POM ($H_3PW_{12}O_{40}$) and a twelve carbon-chain diamine (DD), and they are fabricated on APTES-modified silicon substrates via the LBL self-assembly method. The systematic electron transport study (which was conducted using planar nanoelectrodes) was rendered feasible because of the successful reproduction of the POM-based multilayers with controllable structure. The latter was achieved by the combined (UV/FTIR with XPS) analysis of the film's structural characteristics in function with the fabrication process parameters. Consequently, the control of the electron transport properties of the POM-based multilayers from their structural characteristics presented here makes these molecular materials attractive for use in memory device applications.

RESULTS AND DISCUSSION

POM-Multilayer Fabrication and Spectroscopic Characterization. For the successful fabrication of POM-based multilayers, the LBL self-assembly method, a facile method in producing ultrathin films, was applied. In this method, anionic POMs and cationic DD molecules were deposited alternately forming discrete molecular layers mutually attracted *via* electrostatic interactions. Prior to the multilayer fabrication process the silicon substrate had been functionalized with the adhesion of APTES.[44] Subsequently POMs were deposited forming a monolayer *via* electrostatic interactions with the amine groups of the APTES layer. The whole fabrication process was applied for both single-POM layers and multi-POM layers using appropriate solutions of $H_3PW_{12}O_{40}$ and DD.

After optimization of POM and DD solutions used (the details will be discussed in the next paragraph) controlled and reproducible POM−DD multilayers were obtained as evidenced by both UV absorption and FTIR transmittance studies (Figure 1a,b). In this figure, the first POM-layer is not illustrated, because it is studied in a separate section. Thus, the concentration of POM increased approximately by the same percentage after each POM deposition as presented from the change of the POM absorption peak at 270 nm (Figure 1a). The controlled increase of the POM concentration is also shown from the linear increase of the intensity of this peak with the number of POM-ending bilayers (Figure 1a, right inset). The absorption peak at 270 nm is the characteristic peak of the Keggin structure of $[PW_{12}O_{40}]^{3-}$ anions (Figure 1a, left inset), ascribed to the oxygen-to-metal charge transfer (OMCT: O→W).[14,15,28,45] Further evidence that the concentration of POM increased by about the same percentage after each POM deposition was obtained from the linear increase of the four FTIR bands of POM with the number of POM-ending bilayers (Figure 1b, right inset). The four FTIR bands of the Keggin POM are the following: the first at 793 cm^{-1} attributed to the asymmetric stretching of the W−O_c−W bridge; the second at 895 cm^{-1} attributed to the stretching of the W−O_b−W bridge; the third at 977 cm^{-1} (and 998 cm^{-1}) attributed to the asymmetric stretching of the W−O_d bond; and the fourth at 1079 cm^{-1} attributed to the asymmetric stretching of the P−O_a bond (where O_a is the central oxygen, O_b the bridging oxygen that links two corner-sharing octahedra, O_c the bridging oxygen that links two edge-sharing octahedra, and O_d the terminal oxygen of the POM Keggin structure; left insets of Figure 1a,b).[8,12,13,46–48]

The multilayer fabrication process was optimized after a study on the influence of the composition of the solutions used for POM and DD deposition. The concentrations 0.1 M POM and 0.01 M DD were found to be optimal. Furthermore, the use of acidified aqueous solutions of DD, instead of methanolic solutions of DD, minimized any POM dissolution during DD deposition (details are given in Supporting Information). On the other hand, the pH of both POM- and DD-solution was considered as the key process parameter, because it significantly affected the POM Keggin structures in the

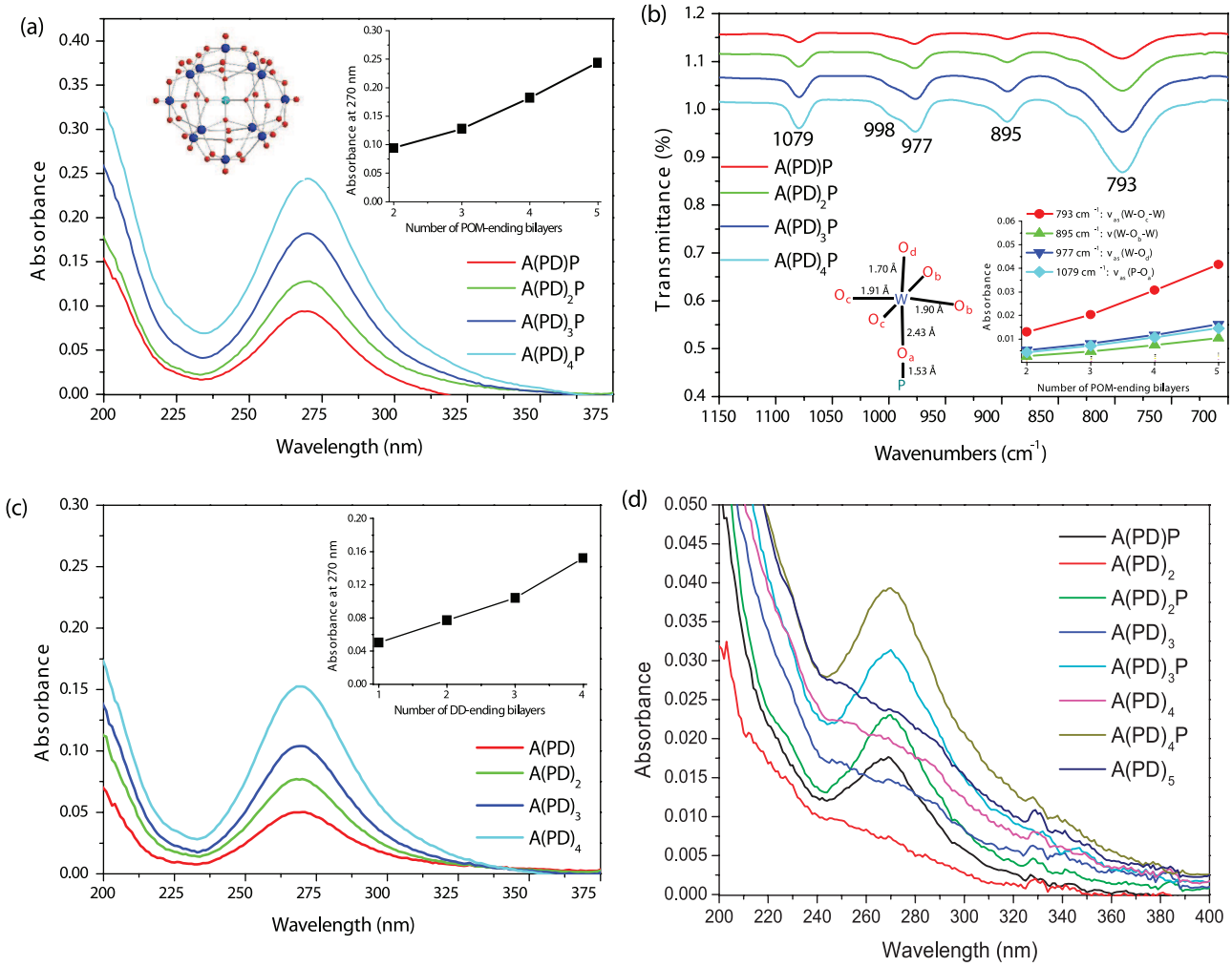

Figure 1. Monitoring of the fabrication of multi-POM layered films (where A = APTES, P = POM, D = DD) with UV and FTIR spectroscopy. (a) UV spectra of POM-ending bilayers at pH 0.5 (the rest process conditions are presented in ref 50); the left inset shows the polyhedral representation of the Keggin structure of $[PW_{12}O_{40}]^{3-}$ anion, the right inset shows the change of the absorption peak intensity of POM at 270 nm with the number of POM-ending bilayers. (b) FTIR spectra of POM-ending bilayers at pH 0.5 as in the panel a case; the left inset shows the structure of a WO_6 octahedron contained in the Keggin structure of $[PW_{12}O_{40}]^{3-}$ anion,[51] the right inset shows the change of the FTIR bands intensity of POM with the number of POM-ending bilayers. (c) UV spectra of DD-ending bilayers at pH 0.5 as in the panel a case. The inset shows the change of the absorption peak intensity of POM at 270 nm with the number of DD-ending bilayers. (d) UV spectra of both POM-ending and DD-ending layers at pH 2 (the rest process conditions are described in ref 52).

multilayers. Thus, it was selected to be equal to 0.5, that is, to fall in the pH stability range of POM in water (pH < 1)[49] in order to avoid structure transformation of POM. Indeed, no structure alteration of POM was observed when both POM and DD were deposited at pH 0.5 as shown from the characteristic POM peak at 270 nm (Figures 1a,c). Also, the controlled increase of the POM concentration during the fabrication process was maintained after each DD deposition at pH 0.5 (Figure 1c, inset). On the other hand, the POM structure changed when DD was deposited at pH 2 (Figure 1d) indicating that not only the pH of POM solution is significant for the maintenance of POM structure, but also the pH of DD solution. In Figure 1d, a shoulder at 270 nm after each DD deposition is depicted indicating alteration of POM structure in all POM layers of the film. In this case, the Keggin structure of $[PW_{12}O_{40}]^{3-}$ anions altered during DD deposition probably with removal of W═O units resulting in a mixture of Keggin structure together with its two "defect" structures of $[P_2W_{21}O_{71}]^{6-}$ and $[PW_{11}O_{39}]^{7-}$ anions.[49] Furthermore, from the comparison of Figure 1 panels a and c the intensity of the 270nm-peak decreased after each DD deposition, a change that could be attributed to the decrease of POM concentration or to alterations in film morphology (without concurrent decrease of POM concentration). The whole issue was subsequently investigated with FTIR and XPS spectroscopy.

Two FTIR spectroscopic techniques: transmission (Figures 1b, 2) and external reflection[53,54] (Figure 3) were applied to study the effect of DD deposition on the POM-based multilayers. It was proved that DD deposition affected the orientation/conformation of POMs, but it did not cause any irreversible alterations in their structure. In addition, it is obvious from Figure 2 that monitoring of one peak of POM for the study of

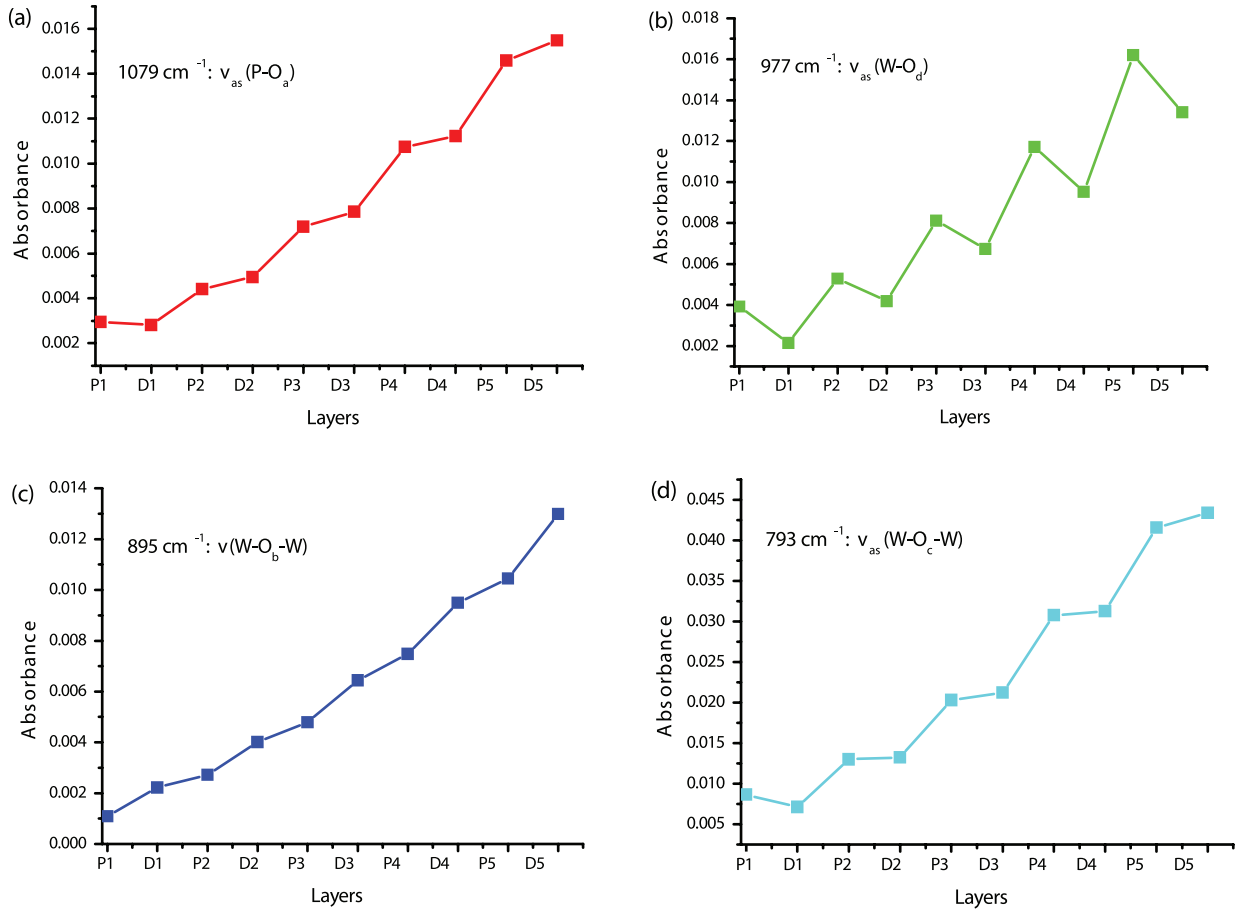

Figure 2. Effect on the intensity of the FTIR transmittance bands of POM at (a) 1079 cm^{-1} (ν_{as} (P−O_a)), (b) 977 cm^{-1} (ν_{as} (W−O_d)), (c) 895 cm^{-1} (ν (W−O_b−W)), and (d) 793 cm^{-1} (ν_{as} (W−O_c−W)), resulting from the DD deposition during the fabrication of five POM-layers. The process conditions were as mentioned in Figure 1a.[50] The POM-based multilayers were fabricated on an APTES adhesion layer.

the effect of DD deposition may not be very safe, a consideration which is also valid for the UV peak of POM (Figure 1c). The central oxygens (O_a) were not affected by DD deposition, as the absorbance intensity of P−O_a bonds (at 1079 cm^{-1}) remained almost unchanged after that step (Figure 2a). From the external oxygens, the terminal oxygens (O_d) were affected significantly by DD deposition, as the absorbance intensity of W−O_d bonds (at 977 cm^{-1}) decreased after that step (Figure 2b). The effect of DD deposition on the O_d oxygens was better supported by external reflection, owing to the higher sensitivity of this technique.[55] In the spectra of this technique, the W−O_d bonds appeared clearly to be weakened after DD deposition, as their band shifted to lower frequencies (*e.g.*, for a 78° angle it was shifted from 995 to 984 cm^{-1}; Figure 3). This behavior of W−O_d bonds was attributed to the increase of the cation size of POMs that were resulted from DD deposition (*i.e.*, replacement of three protons of POM by three protonated DD counterions), an explanation which is in good agreement with a previous finding.[46] On the other hand, the two categories of bridging oxygens exhibited diverse behavior toward DD deposition. The oxygens that bridge corner-sharing octahedra (O_b) were affected by DD adsorption, whereas the oxygens that bridge edge-sharing octahedra (O_c) were not influenced. This was documented from the increase of the absorbance intensity of W−O_b−W bridges (at 895 cm^{-1}) and the nonchange of the absorbance intensity of W−O_c−W bridges (at 793 cm^{-1}) that resulted from DD deposition, respectively (Figure 2c,d). The effect of DD deposition on O_b oxygens could be ascribed to deprotonation of O_b oxygens caused by DD adsorption, since the bridging oxygens are the preferred nucleophilic sites of POMs.[56] In contrast, the diverse behavior of O_c bridging oxygens in relation to O_b bridging oxygens toward DD deposition could be possibly attributed to their different W−O−W angle (126° and 152°, respectively),[48] but the whole issue needs further investigation.

Angle resolved XPS at three different angles (0, 60, and 75 °) was employed to detect the elemental surface composition of POM−DD multilayers, a study which led to the following basic findings (for more details see Supporting Information): (a) POM and DD form discrete layers with thicknesses around 1.7 and 1 nm, respectively, according to variation analysis of all element intensities at all three take off angles. (b) The ad-

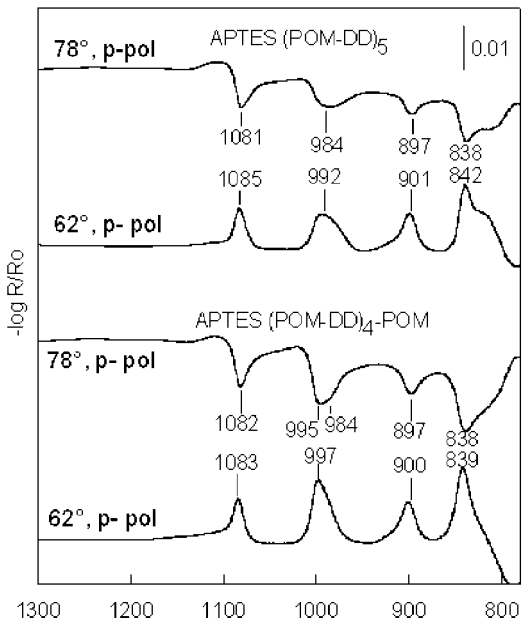

Figure 3. External reflection spectra of POM-ending and DD-ending multilayers recorded for p-polarization at 62° and 78° incident angles. (The unit of intensity is defined as $-\log(R/R_0)$, where R and R_0 are the reflectivities of the system with and without the investigated adsorption layer, respectively). The process conditions were as mentioned in Figure 1a,[50] whereas the POM-based multilayers were fabricated on an APTES adhesion layer.

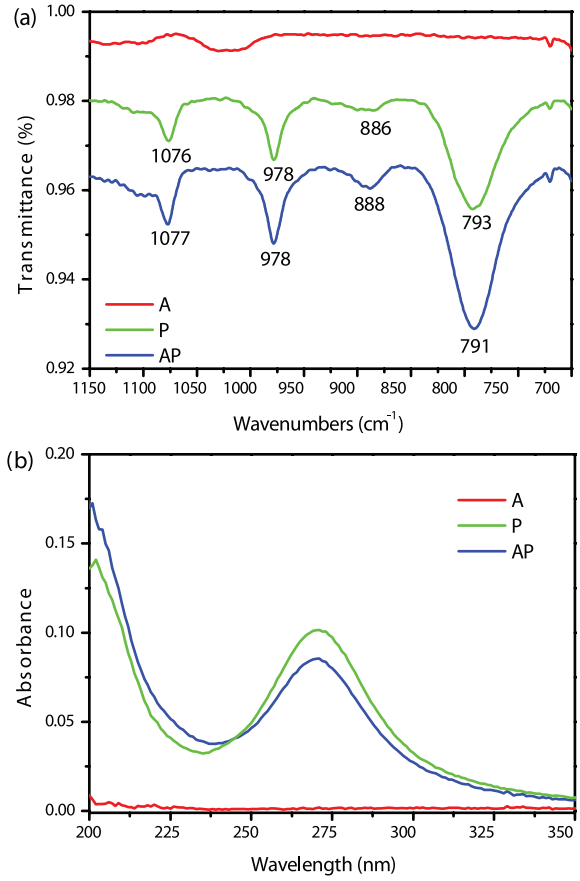

Figure 4. FTIR transmittance spectra (a) and UV spectra (b) of a single-POM layer either deposited on an APTES adhesion layer or deposited directly on the substrate (the APTES adhesion layer is also presented). The substrate was a silicon wafer for the FTIR spectra and a quartz slide for the UV spectra. (The POM deposition conditions are described in ref 50).

sorption of DD layer results in a discontinuous "patch-like" surface morphology with a large distance between POM aggregates, whereas uniform films were created when POM was the outermost layer. This was deduced from the significant signal from the substrate (Si^0 and SiO lines) detected when DD was the last layer, but not when POM was the outermost layer. (c) The adsorbed DD molecules interact with POMs mainly *via* one protonated amino group ($-NH_3^+$) of DD, whereas the second $-NH_3^+$ group of DD interacts with chlorine counterion ($-NH_3^+Cl^-$). This was documented from the detection of a considerable chlorine ion signal (Cl 2p line) when DD was the last layer, while no chorine signal was observed when POM was the outermost layer. (d) Strong electrostatic interactions between POM and DD take place, as the major N 1s and P 2p lines are shifted to higher positions. (e) These POM−DD electrostatic interactions in the last (fifth) bilayer are very similar with those in the first bilayer indicating that the same reaction mechanism takes place in each step of the multilayer process, a fact that was substantiated by the comparison of the respective positions of the major N 1s and P 2p lines. These XPS observations are in good agreement with the FTIR spectroscopic findings.

Single-POM Layer Fabrication and Spectroscopic Characterization. Having extensively used the APTES adhesion layer in the fabrication of multi-POM layers, the role of that layer was obviously an issue that needed investigation. To have a clear picture of that role, the effect of the APTES adhesion layer on a single-POM layer was studied. Thus, two single-POM layers, one deposited on the APTES adhesion layer and another deposited directly on a substrate (the latter for control reasons), were investigated with FTIR and UV spectroscopy (Figure 4). From this study, it was shown that the APTES adhesion layer was necessary for the controlled and reproducible deposition of POMs in a single layer. In particular, the POM concentration of the single-POM layer deposited on the APTES layer was reproducible and usually higher than the POM concentration of the single-POM layer deposited directly on a silicon wafer (Figure 4a). On the other hand, in control experiments we observed that POMs were capable of being adsorbed directly on a silicon wafer (actually on its native oxide; Figure 4a) and a quartz surface (Figure 4b). The POM adsorption in this case was irreproducible (the POM concentration without the APTES layer was lower (Figure 4a) and higher (Figure 4b) than the POM concentration with the APTES layer) and depended strongly on the substrate. For this reason in all samples used subsequently in the electrical characterization the APTES-treatment was used. In addition, the widening of the 270 nm peak of POM observed when POMs deposited on the APTES layer (Figure 4b) resulted from the

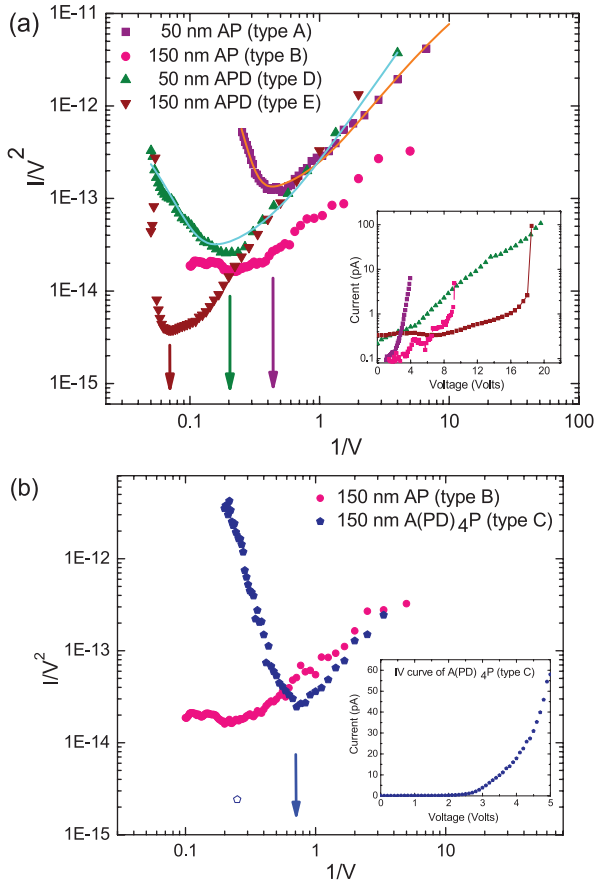

Figure 5. (a) Comparison of FN curves between POM-ending single-layers (types A and B) and DD-ending single-layers (types D and E) for two different electrode gaps (50 and 150 nm). Solid lines correspond to theoretical fits according to Simmons's model. Arrows indicate the onset of FN tunneling. The inset shows the direct *I*−*V* curves. (b) Comparison of FN curves between a POM-ending single-layer (type B) and a POM-ending five-layer (type C) for an electrode gap of 150 nm. Arrow indicates the bias at which onset of FN tunneling takes place for sample type C, while FN tunneling never occurs for sample type B. The inset shows the direct *I*−*V* curve of sample type C.

different type of interactions between POM and APTES layer in relation to the interactions between POM and quartz surface. Finally, the single-POM layer deposited on the APTES layer exhibited adequate surface coverage.

From the XPS study of single-POM layers the following observations were made (for more details see Supporting Information): (a) The silicon substrate was covered by a 0.75 nm thick silicon oxide layer as deduced from the position of Si 2p line. (b) Adsorption of POM directly on a silicon wafer produced a nonuniform POM layer with 1.6 nm thickness, as the O 1s line of silicon oxide (from substrate) had almost twice intensity as that of tungsten oxide (from POM). This is in agreement with the reproducibility problem found in the previous UV/FTIR study of single-POM layers. (c) APTES adsorption on silicon substrate produced a uniform layer, which significantly attenuated the signal from substrate. On top of this layer, both amino (NH_2) and protonated amino (NH_3^+) groups were detected having the same

TABLE 1. Structure of the Films Used in the Electrical Characterization[a]

sample type	number of layers	ending layer	sample description	interelectrode distance (nm)
A	1	POM	AP	50
B	1	POM	AP	150
C	5	POM	$A(PD)_4P$	150
D	1	DD	APD	50
E	1	DD	APD	150

[a]For simplicity the description of the samples is given with the initial letter of each layer, where A = APTES, P = POM, D = DD. The process conditions were the optimal conditions of Figure 1a.[50] Electrode material is Al.

concentration, due to the neutral pH of the APTES solution used. The presence of NH_3^+ group was supported by the observation of a chlorine ion signal (Cl 2p line) which is the counterion of NH_3^+. (d) Adsorption of POM on APTES layer produced a continuous compact layer which tremendously attenuated the signal from the silicon substrate. Strong electrostatic interactions between APTES and POM were observed, as confirmed by the high position of both the N 1s and P 2p lines. The last finding is also in agreement with the previous UV/FTIR study of single-POM layers.

Electron Transport Study on POM-Layered Structures. The electron transport mechanisms of POM layers were studied in relation to three structural parameters: (a) the number of layers (1 or 5 layers), (b) the nature of the final layer (POM or DD), and (c) the gap width between electrodes (50 or 150 nm) (Table 1). The obtained *I*−*V* curves were studied under the Fowler−Nordheim (FN) representation and fitted according to the Simmons tunneling model.[57]

The results obtained for single POM layers as a function of the interelectrode distance and the nature of the topmost layer are presented in Figure 5a. At low voltage bias two mechanisms, percolation and tunneling, coexist in all cases, as resulted from the linearity of all the FN curves ($(1/V^2) \propto (1/V)$). At high voltage bias, FN tunneling dominates (as indicated by the exponential dependence of I/V^2 over $1/V$), except for POM-ending films with 150 nm gap width (type B) for which tunneling never sets off. The onset of FN tunneling for the other three sample types occurs at different biases, the lowest of which corresponded to type A (POM-ending film, 50 nm gap width), the intermediate one to type D (DD-ending film, 50 nm gap width), and the highest one to type E (DD-ending film, 150 nm gap width). The onset of FN tunneling for DD-ending films (type D) occurs at 1 order of magnitude higher voltage bias than the one for POM-ending films (type A), an observation which is also supported from the following theoretical fitting results:[57−59] (a) the effective barrier width for DD-ending films is higher than the one for POM-ending films ($s_D > s_A$), whereas the effective barrier height is lower ($\varphi_D < \varphi_A$); (b) the tunneling probability, ($p_{tun} \propto \exp(-s\sqrt{\varphi})$) for DD-ending films is at least 2 orders of

magnitude lower than the one for POM-ending films (1.5×10^{-4} *vs* 0.05). On the other hand, when more layers are added to the POM-ending films with 150 nm gap width, FN tunneling dominates and the onset occurs at bias values in the same order of magnitude as for sample type A as shown in Figure 5b.

The *I*−*V* curves combined with the XPS and UV/FTIR analysis provided the necessary information to develop a model about the electron transport mechanisms involved in each case. At the low-voltage regime where percolation and tunneling coexist, POMs act as electron traps. In this case electrons follow a "random-walk" path among energetically favorable sites (POMs) until they reach the other electrode, whereas the whole region simultaneously poses a tunneling barrier. At the high-voltage regime, the three structural parameters of the POM layers become important and affect considerably which transport mechanism will dominate in each case (Figure 6). In the POM-ending films (which exhibited uniform coverage according to XPS and UV/FTIR analysis) electron transport occurs through individual POM molecules: (a) When the gap between the electrodes is relatively short (50 nm) and the applied bias sufficient, electrons tunnel to the other electrode. (b) When the gap becomes relatively wide (150 nm), the percolation threshold voltage increases and percolation dominates over tunneling. (c) On the other hand, in the DD-ending films (which presented a "patchlike" morphology according to XPS study) electrons tunnel to the other electrode through the POM-aggregates formed, irrespectively of the gap width. This behavior can be attributed to the fact that the POM-aggregates act as more effective electron traps than individual POM molecules. (d) Finally, when more layers are added to the structure, alternative paths are offered to the electrons tunneling from POM molecule to POM molecule and FN tunneling can be realized even at relatively wide gaps. This tunneling behavior could be rationalized with the assumption that the addition of POM layers in the film increases the probability that an electron can successfully find its way through the film before dispensing its kinetic energy.

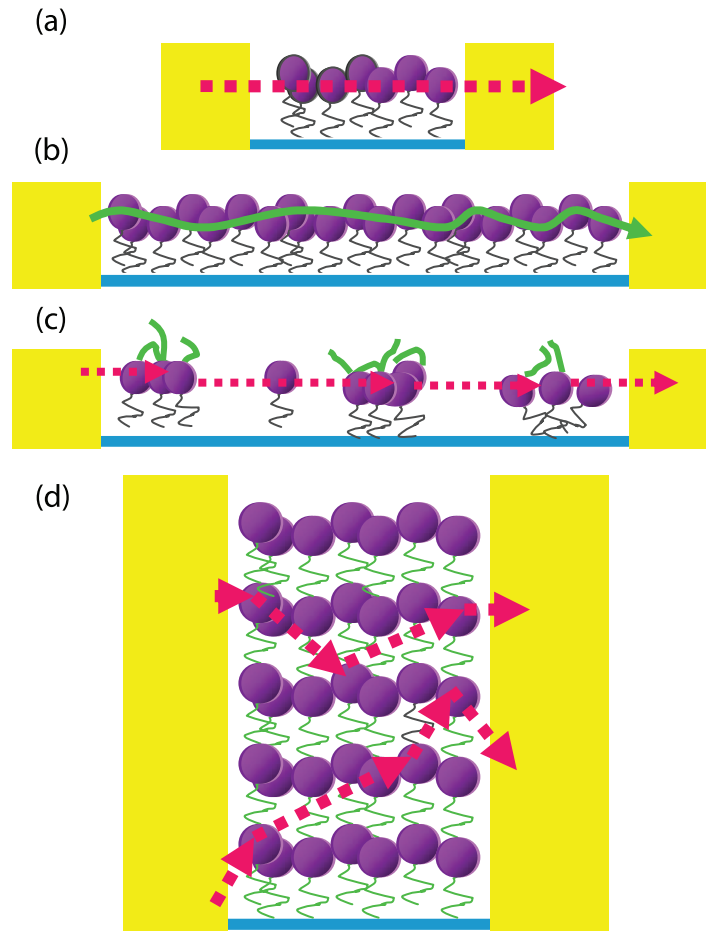

Figure 6. Schematic diagram of the transport mechanism model through the various film types at the high-voltage regime. For POM-ending films electron transport occurs through POM molecules: (a) When the gap between the electrodes is relatively short (50 nm) and the applied bias sufficient, the electrons can tunnel to the other electrode. (b) When the gap becomes relatively wide (150 nm), the electrons can never acquire enough energy to tunnel through to the other electrode and percolation dominates. (c) In case of DD-ending films the electrons tunnel through the aggregates formed (due to the presence of the DD final layer) irrespective of gap width. (d) When more layers are added to the structure, alternative paths are offered to the electrons and FN tunneling can be realized even at relatively wide gaps.

CONCLUSIONS

The LBL self-assembly method has been successfully applied for the fabrication of hybrid organic–inorganic molecular layers based on POMs. FTIR and UV spectroscopy in conjunction with XPS guided the optimization of the fabrication process parameters (concentrations of POM and DD solutions, nature of DD solvent, and pH of both POM- and DD-solution) and allowed the reproducible fabrication of well-characterized single-layered and multilayered POM-based films. In addition, electrical measurements and subsequent theoretical analysis revealed the electron transport mechanisms of the produced films as a function of their structural properties. Consequently, a method was established *via* which one can reproducibly fabricate POM-based molecular films with electrical properties fine-tuned *via* their structure and tailored for a novel molecular electronics material.

EXPERIMENTAL SECTION

Materials. 12-Tungstophosphoric acid hydrate (POM, $H_3PW_{12}O_{40} \cdot xH_2O$, obtained from Aldrich), 3-aminopropyl triethoxysilane (APTES, obtained from Aldrich), and 1,12-diaminododecane (DD, obtained from Fluka) were of analytical grade and used without further purification. Hydrochloric acid and sulfuric acid (both obtained from Aldrich) were also of analytical grade and they were used for the pH adjustment of the deposition solutions. Deionized water with a resistivity of 15 MΩ cm^{-1} prepared from the Milli-RO plus 90 apparatus (Millipore)

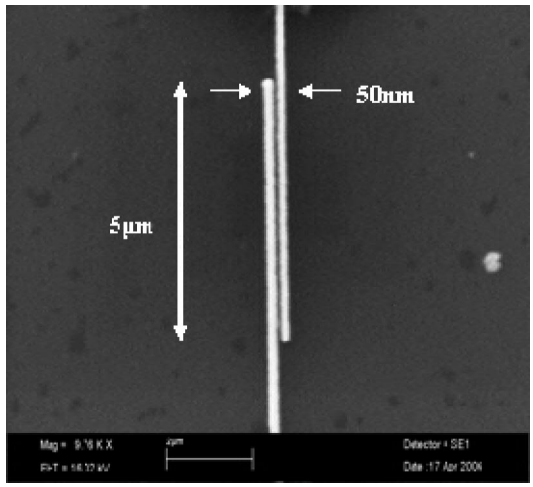

Figure 7. SEM image of the planar interdigitated Au electrodes.

was used in all the experiments. The substrates used in the multilayer fabrication varied according to the characterization method applied; thus, quartz slides were used for the UV study and silicon wafers were used for the FTIR, SEM, and XPS studies. The substrates were used after cleaning with piranha solution (H_2O_2:H_2SO_4, 1:1 v/v). Electrical characterization of the hybrid POM-based multilayers was performed through the use of planar interdigitated Au electrodes on SiO_2-covered silicon wafers patterned by e-beam lithography using lift-off. The length of the parallel electrodes was 5 μm and their distance varied between 50 and 150 nm (Figure 7). This particular geometry of planar electrodes was selected because of the homogeneity of the electric field obtained this way.

Film Fabrication. The typical process for the fabrication of POM−DD multilayer films was the following. Initially, the substrates (quartz and Si wafers) were incubated in an APTES aqueous solution (2% v/v, pH ≈ 7) at room temperature (rt) for 20 min, rinsed cautiously with water, and dried with nitrogen stream. Then, they were treated thermally at 120 °C for 20 min.[44] Subsequently they were incubated in a POM aqueous solution (concentration range 0.1–10^{-3} M) at rt for 20 min, rinsed with HCl aqueous solution, and dried with nitrogen stream. Afterward, they were incubated in a DD aqueous solution (concentration range 0.01 − 10^{-4} M) at rt for 20 min, rinsed with HCl aqueous solution, and dried with nitrogen stream. The alternate incubations in POM and DD solutions along with the intermediate rinsing and drying steps were continued until the fabrication of the appropriate multilayer film. The monolayers were deposited on both sides of the substrates.

Characterization Methods. UV–vis absorption spectra were obtained on a Perkin-Elmer UV–vis Lambda 40 spectrophotometer. FTIR transmittance spectra were recorded on a Bruker, Tensor 27 spectrometer using 128 scans at 4 cm^{-1} spectral resolution. FTIR external reflection spectra were recorded on a Bruker IFS55 spectrometer equipped with a MCT detector, a variable angle reflectance accessory (Seagull), a wire-grid polarizer (Harrick Scientific Co) for the production of p- or s-polarized light. FTIR external reflection spectra were obtained using 200 scans at 4 cm^{-1} resolution with a Blackman–Harris, three-term apodization.[53,54] XPS spectra were obtained with an AXIS NOVA spectrometer (Kratos Analytical, Manchester, U.K.) using monochromatic Al Kα (hv = 1486.6 eV) radiation. The carbon C1s line with position at 284.6 eV was used as a reference to correct the charging effect.[60] To study the molecular structure of the top surface layers, angle-resolved XPS was applied and spectra were recorded for three takeoff angles (0, 60, and 75°).[61] Scanning electron micrographs were obtained on a HITACHI S-2500 scanning electron microscope equipped with an EDS super Quantum Delta spectrometer and a detector of retro-diffused electrons. Electrical measurements were carried out at ambient conditions employing a Hewlett-Packard parameters analyzer (HP 4140B).

Acknowledgment. This work was funded from the "TASNANO" project (FP6-NMP 516865 project) of the European Community. The authors thank Dr. D. Velessiotis for the fabrication of the electrodes used in the electrical characterization of the hybrid POM-based multilayers.

Supporting Information Available: Optimization of the concentrations of deposition solutions, study of the nature of DD solvent, FTIR peaks of POM after each deposition step, and a detailed XPS study of both single-layers and multilayers. This material is available free of charge *via* the Internet at http://pubs.acs.org.

REFERENCES AND NOTES

1. Akkerman, H. B.; Blom, P. W. M.; de Leeuw, D. M.; de Boer, B. Towards Molecular Electronics with Large-Area Molecular Junctions. *Nature* **2006**, *441*, 69–72.
2. Blum, A. S.; Kushmerik, J. G.; Long, D. P.; Patterson, C. H.; Yang, J. C.; Henderson, J. C.; Yao, Y.; Tour, J. M.; Shashidhar, R.; Ratna, B. R. Molecularly Inherent Voltage-Controlled Conductance Switching. *Nat. Mater.* **2005**, *4*, 167–172.
3. He, J.; Chen, B.; Flatt, A. K.; Stephenson, J. J.; Doyle, C. D.; Tour, J. M. Metal-Free Silicon-Molecule-Nanotube Testbed and Memory Device. *Nat. Mater.* **2006**, *5*, 63–68.
4. Dholakia, G. R.; Meyyappan, M.; Facchetti, A.; Marks, T. J. Monolayer to Multilayer Nanostructural Growth Transition in N-Type Oligothiophenes on Au(111) and Implications for Organic Field-Effect Transistor Performance. *Nano Lett.* **2006**, *6*, 2447–2455.
5. Cheng, J.; Robinson, D. B.; Cicero, R. L.; Eberspacher, T.; Barrelet, C. J.; Chidsey, C. E. D. Distance Dependence of the Electron-Transfer Rate Across Covalently Bonded Monolayers on Silicon. *J. Phys. Chem. B* **2001**, *105*, 10900–10904.
6. Long, D.-L.; Burkholder, E.; Cronin, L. Polyoxometalate Clusters, Nanoclusters and Materials: From Self-Assembly to Designer Materials and Devices. *Chem. Soc. Rev.* **2007**, *36*, 105–121.
7. Duclusaud, H.; Borshch, S. A. Electron Delocalization and Magnetic State of Doubly-Reduced Polyoxometalates. *J. Am. Chem. Soc.* **2001**, *123*, 2825–2829.
8. Maestre, J. M.; Lopez, X.; Bo, C.; Poblet, J.-M.; Casañ-Pastor, N. Electronic and Magnetic Properties of α-Keggin Anions: A DFT study of $[XM_{12}O_{40}]^{n-}$, (M = W, Mo; X = Al^{III}, Si^{IV}, P^{V}, Fe^{III}, Co^{II}, Co^{III}) and $[SiM_{11}VO_{40}]^{m-}$ (M = Mo and W). *J. Am. Chem. Soc.* **2001**, *123*, 3749–3758.
9. Waters, T.; Huang, X.; Wang, X.-B.; Woo, H.-K.; O'Hair, R. A. J.; Wedd, A. G.; Wang, L.-S. Photoelectron Spectroscopy of Free Multiply Charged Keggin Anions α-$[PMo_{12}O_{40}]^{3-}$ (M = Mo, W) in the Gas Phase. *J. Phys. Chem. A* **2006**, *110*, 10737–10741.
10. Pope, M. T. *Heteropoly and Isopoly Oxometalates;* Springer-Verlag: Berlin, 1983; pp 15–32.
11. Pope, M. T.; Muller, A. Polyoxometalate Chemistry: An Old Field with New Dimensions in Several Disciplines. *Angew. Chem., Int. Ed. Engl.* **1991**, *30*, 34–48.
12. Keggin, J. F. Structure of the Molecule of 12-Phosphotungstic Acid. *Nature* **1933**, *131*, 908–909.
13. Keggin structure has overall T_d symmetry. It is based on a central PO_4 tetrahedron surrounded by twelve WO_6 octahedra arranged in four groups of three edge-shared octahedra, W_3O_{13}. These groups are linked by shared corners to each other and to the central PO_4 tetrahedron. All WO_6 octahedra of Keggin structure have one terminal M-O_d bond (type I octahedra according to the Pope classification; see refs 10, 11).
14. Hiskia, A.; Mylonas, A.; Papakonstantinou, E. Comparison of the Photoredox Properties of Polyoxometallates and Semiconducting Particles. *Chem. Soc. Rev.* **2001**, *30*, 62–69.
15. Papaconstantinou, E. Photochemistry of Polyoxometallates of Molybdenum and Tungsten and/or Vanadium. *Chem. Soc. Rev.* **1989**, *18*, 1–31.
16. This electron storage capacity is a general characteristic of POMs with type I octahedra, and it is attributed to the nonbonding character of the lowest unoccupied

molecular orbitals (LUMOs) of these octahedra. Since the metal ions in the oxidized type I octahedra have d^0 electronic configuration, the LUMOs are mainly composed of nonbonding, metal d_{xy} orbitals with low contribution of antibonding oxygen orbitals, whereas the highest occupied molecular orbitals (HOMOs) are mainly composed of oxygen 2p orbitals (refs 10, 11, 17, 19).

17. Poblet, J. M.; López, X.; Bo, C. Ab Initio and DFT Modelling of Complex Materials: Towards the Understanding of Electronic and Magnetic Properties of Polyoxometalates. *Chem. Soc. Rev.* **2003**, *32*, 297–308.
18. Suaud, N.; Gaita-Ariño, A.; Clemente-Juan, J. M.; Sánchez-Marín, J.; Coronado, E. Electron Delocalization in Mixed-Valence Keggin Polyoxometalates. Ab Initio Calculation of the Local Effective Transfer Integrals and Its Consequences on the Spin Coupling. *J. Am. Chem. Soc.* **2002**, *124*, 15134–15140.
19. López, X.; Bo, C.; Poblet, J. M. Electronic Properties of Polyoxometalates: Electron and Proton Affinity of Mixed-Addenda Keggin and Wells-Dawson Anions. *J. Am. Chem. Soc.* **2002**, *124*, 12574–12582.
20. Xu, B.; Lu, M.; Kang, J.; Wang, D.; Brown, J.; Peng, Z. Synthesis and Optical Properties of Conjugated Polymers Containing Polyoxometalate Clusters as Side-Chain Pendants. *Chem. Mater.* **2005**, *17*, 2841–2851.
21. Lu, M.; Xie, B.; Kang, J.; Chen, F.-C.; Yang, Y.; Peng, Z. Synthesis of Main-Chain Polyoxometalate-Containing Hybrid Polymers and Their Applications in Photovoltaic Cells. *Chem. Mater.* **2005**, *17*, 402–408.
22. Wang, L.; Xiao, D.; Wang, E.; Xu, L. Electrochemistry of ITO Electrode Modified by Multilayer Ultrathin Films Based on Crown-Shaped Polyoxomolybdate. *J. Colloid Interface Sci.* **2005**, *285*, 435–442.
23. Zhang, G.; Yang, W.; Yao, J. Thermally Enhanced Visible-Light Photochromism of Phosphomolybdic Acid-Polyvinylpyrrolidone Hybrid Films. *Adv. Funct. Mater.* **2005**, *15*, 1255–1259.
24. Nelson, C. B.; Vyas, R. N.; Mou, Y.; Li, K.; Rabalais, J. W.; Irwin, G. M.; Wang, B. Doping Poly(*p*-Phenylene Vinylene) with Phosphomolybdate through Layer-by-Layer Fabrication for Optoelectronic Applications. *J. Appl. Phys.* **2007**, *102*, 0943091–0943096.
25. Gao, G.; Xu, L.; Wang, W.; Wang, Z.; Qiu, Y.; Wang, E. Electrchromic Multilayer Films Based on Trilacunary Dawson-Type Polyoxometalate. *Electrochim. Acta* **2005**, *50*, 1101–1106.
26. Lehmann, J.; Gaita-Arino, A.; Coronado, E.; Loss, D. Spin Qubits with Electrically Gated Polyoxometalate Molecules. *Nat. Nanotechnol.* **2007**, *2*, 312–317.
27. Coronado, E.; Gomez-Garcia, C. J. Polyoxometalate-Based Molecular Materials. *Chem. Rev.* **1998**, *98*, 273–296.
28. Yamase, T. Photo- and Electrochromism of Polyoxometalates and Related Materials. *Chem. Rev.* **1998**, *98*, 307–325.
29. Jiang, M.; Wang, E.; Kang, Z.; Lian, S.; Wu, A.; Li, Z. In Situ Controllable Synthesis of Polyoxometalate Nanoparticles in Polyelectrolyte Multilayers. *J. Mater. Chem.* **2003**, *13*, 647–649.
30. Shen, Y.; Liu, J.; Jiang, J.; Liu, B.; Dong, S. Fabrication of a Metalloporphyrin-Polyoxometalate Hybrid Film by a Layer-by-Layer Method and Its Catalysis for Hydrogen Evolution and Dioxygen Reduction. *J. Phys. Chem. B* **2003**, *107*, 9744–9748.
31. Wang, Y.; Hu, C. Layer-by-Layer Self-Assembly of Dye-Polyoxometalate Multilayer Composite Films and Their Fluorescent Properties. *Thin Solid Films* **2005**, *476*, 84–91.
32. Wang, K.-Z.; Gao, L.-H. Hybrid Self-Assembled Multilayer Film Formed by Alternating Layers of $H_4SiW_{12}O_{40}$ and 1,10-Diaminodecane (DAD). *Mater. Res. Bull.* **2002**, *37*, 2447–2451.
33. Oh, S.-Y.; Yun, Y.-J.; Kim, D.-Y.; Han, S.-H. Formation of a Self-Assembled Monolayer of Diaminododecane and a Heteropolyacid Monolayer on the ITO Surface. *Langmuir* **1999**, *15*, 4690–4692.
34. Decher, G. Fuzzy Nanoassemblies: Towards Layered Polymeric Multicomposites. *Science* **1997**, *277*, 1232–1237.
35. Bryce, M. R.; Petty, M. C. Electrically Conductive Langmuir-Blodgett Films of Charge-Transfer Materials. *Nature* **1995**, *374*, 771–776.
36. Clemente-León, M.; Coronado, E.; Gómez-García, C. J.; Mingotaud, C.; Ravaine, S.; Romualdo-Torres, G.; Delhaès, P. Polyoxometalate Monolayers in Langmuir-Blodgett Films. *Chem. Eur. J.* **2005**, *11*, 3979–3987.
37. Bidan, G.; Jalaguier, E. Polyoxometalates in Memory Devices. International Patent Application, (PCT), WO 2007/015010 A1, 07/02/2007.
38. Glezos, N.; Argitis, P.; Velessiotis, D.; Diakoumakos, C. D. Tunneling Transport in Polyoxometalate Based Composite Materials. *Appl. Phys. Lett.* **2003**, *83*, 488–490.
39. Velessiotis, D.; Glezos, N.; Ioannou-Sougleridis, V. Tungstate Polyoxometalates as Active Components of Molecular Devices. *J. Appl. Phys.* **2005**, *98*, 0845031–0845034.
40. Alivisatos, A. P. Semiconductor Clusters, Nanocrystals, and Quantum Dots. *Science* **1996**, *271*, 933–937.
41. Kavan, L.; Dunsch, L. Spectroelectrochemistry of Carbon Nanostructures. *Chem. Phys. Chem.* **2007**, *8*, 974–998.
42. Wilcoxon, J. P.; Abrams, B. L. Synthesis, Structure and Properties of Metal Nanoclusters. *Chem. Soc. Rev.* **2006**, *35*, 1162–1194.
43. Glezos, N.; Douvas, A. M.; Argitis, P.; Saurenbach, F.; Chrost, J.; Livitsanos, C. Electrical Characterization of Molecular Monolayers Containing Tungsten Polyoxometalates. *Microelectron. Eng.* **2006**, *83*, 1757–1760.
44. Misiakos, K.; Kakabakos, S. E.; Petrou, P. S.; Ruf, H. H. A Monolithic Silicon Optoelectronic Transducer as a Real-Time Affinity Biosensor. *Anal. Chem.* **2004**, *76*, 1366–1373.
45. The OMCT absorption band is due to the promotion of electrons from the high energy electronic states of HOMO to the low energy electronic states of LUMO of POM.
46. Rocchiccioli-Deltcheff, C.; Fournier, M.; Franck, R.; Thouvenot, R. Vibrational Investigations of Polyoxometalates. 2. Evidence for Anion-Anion Interactions in Molybdenum(VI) and Tungsten(VI) Compounds Related to the Keggin Structure. *Inorg. Chem.* **1983**, *22*, 207–216.
47. Thouvenot, R.; Fournier, M.; Franck, R.; Rocchiccioli-Deltcheff, C. Vibrational Investigations of Polyoxometalates. 3. Isomerism in Molybdenum(VI) and Tungsten(VI) Compounds Related to the Keggin Structure. *Inorg. Chem.* **1984**, *23*, 598–605.
48. Ganapathy, S.; Fournier, M.; Paul, J. F.; Delevoye, L.; Guelton, M.; Amoureux, J. P. Location of Protons in Anhydrous Keggin Heteropolyacids $H_3PMo_{12}O_{40}$ and $H_3PW_{12}O_{40}$ by $^1H\{^{31}P\}/^{31}P\{^1H\}$ REDOR NMR and DFT Quantum Chemical Calculations. *J. Am. Chem. Soc.* **2002**, *124*, 7821–7828.
49. Zhu, Z.; Tain, R.; Rhodes, C. A Study of the Decomposition Behaviour of 12-Tungstophosphate Heteropolyacid in Solution. *Can. J. Chem.* **2003**, *81*, 1044–1050.
50. The process conditions in the (a−c) cases of Figure 1 were the optimal conditions found: POM 0.1 M, aq, pH 0.5, rt, 20 min (rinsing: HCl 0.3 M, aq, pH 0.5); DD 0.01 M, aq, HCl 0.3 M, pH 0.5, rt, 20 min (rinsing: HCl 0.3 M, aq, pH 0.5). The POM-based multilayers were fabricated on an APTES adhesion layer.
51. The distances (in Å) of the bonds in Figure 1b are experimental values obtained from refs 8, 48.
52. The process conditions in the (d) case of Figure 1 were: POM 0.01 M, aq, pH 1.5, rt, 20 min (rinsing: water, pH ≈ 7); DD 9×10^{-3} M, aq, H_2SO_4 5×10^{-3} M, pH 2, rt, 20 min (rinsing: water, pH ≈ 7). The POM-based multilayers were fabricated on an APTES adhesion layer.
53. Mielczarski, J. A. External Reflection Infrared Spectroscopy at Metallic, Semiconductor, and Nonmetallic Substrates. 1. Monolayer Films. *J. Phys. Chem.* **1993**, *97*, 2649–2663.
54. Mielczarski, J. A.; Mielczarski, E. Determination of Molecular Orientation and Thickness of Self-Assembled

Monolayers of Oleate on Apatite by FTIR Reflection Spectroscopy. *J. Phys. Chem.* **1995**, *99*, 3206–3217.
55. In the transmission method the electric vectors of incident beam are positioned only parallel to the surface plane of sample. Hence, only the surface molecular groups that have dipole moments parallel to sample interface could produce an absorbance band. When the external reflection method is used there are electric vectors at the interface which are parallel to the interface (as in transmission method) and vertical to the interface depending on the angle of incident beam and polarization.
56. Fernández, J. A.; López, X.; Poblet, J. M. A DFT Study on the Effect of Metal, Anion Charge, Heteroatom and Structure upon the Relative Basicities of Polyoxoanions. *J. Mol. Catal. A* **2007**, *262*, 236–242.
57. Simmons, J. G. Generalized Formula for the Electric Tunnel Effect between Similar Electrodes Separated by a Thin Insulating Film. *J. Appl. Phys.* **1963**, *34*, 1793–1803.
58. Braun, D. Electronic Injection and Conduction Processes for Polymer Devices. *J. Polym. Sci., Part B* **2003**, *41*, 2622–2629.
59. Wang, W.; Lee, T.; Reed, M. A. Mechanism of Electron Conduction in Self-Assembled Alkanethiol Monolayer Devices. *Phys. Rev. B* **2003**, *68*, 0354161–0354167.
60. More details about the XPS spectra obtained are the following: The kinetic energy of the photoelectrons was determined with the hemispheric analyser set to the pass energy of 160 eV for wide scan spectra and 20 eV for high resolution spectra. The electrostatic charge effect of the sample was overcompensated by means of the low-energy electron source working in combination with a magnetic immersion lens. Quantitative elemental compositions were determined from peak areas using experimentally determined sensitivity factors and the spectrometer transmission function. Spectrum background was subtracted according to Shirley. The high resolution spectra were analysed by means of spectra deconvolution software (Vision 2, Kratos Analytical, U.K.).
61. The take-off angle is defined as the angle between the normal to the surface of the sample and the electron optical axis of the spectrometer. The effective information depth, varies according to $d = d_0 \cos \theta$, where d_0 is the maximum information depth ($d_0 \approx 10$ nm for the C1s line by employing an Al Kα source).